Schemes for Tracking Resonance Frequency for Micro- and Nanomechanical Resonators

Hajrudin Bešić,[1,*] Alper Demir,[2] Johannes Steurer,[1] Niklas Luhmann,[1] and Silvan Schmid[1]

[1] *Institute of Sensor and Actuator Systems, TU Wien, Gusshausstrasse 27–29, Vienna 1040, Austria*

[2] *Department of Electrical Engineering, Koç University, Istanbul 34450, Turkey*

(Received 13 May 2023; accepted 13 July 2023; published 9 August 2023)

Nanomechanical resonators can serve as high-performance detectors and have the potential to be widely used in industry for a variety of applications. Most nanomechanical-sensing applications rely on detecting changes of resonance frequency. In commonly used frequency-tracking schemes, the resonator is driven at or close to its resonance frequency. Closed-loop systems can continually check whether the resonator is at resonance and adjust the frequency of the driving signal accordingly. In this work, we study three resonance-frequency-tracking schemes, a feedback-free (FF) scheme, a self-sustaining oscillator (SSO) scheme, and a phase-locked loop oscillator (PLLO) scheme. We improve and extend the theoretical models for the FF and the SSO tracking schemes and test the models experimentally with a nanoelectromechanical system (NEMS) resonator. We employ an SSO architecture with a pulsed positive-feedback topology and compare it to the commonly used PLLO and FF schemes. We show that all tracking schemes are theoretically equivalent and that they all are subject to the same speed versus accuracy trade-off characteristics. In order to verify the theoretical models, we present experimental steady-state measurements for all of the tracking schemes. The frequency stability is characterized by computing the Allan deviation. We obtain almost perfect correspondence between the theoretical models and the experimental measurements. These results show that the choice of the tracking scheme is dictated by cost, robustness, and usability in practice as opposed to fundamental theoretical differences in performance.

DOI: 10.1103/PhysRevApplied.20.024023

I. INTRODUCTION

Micro- and nanomechanical resonators are exceptional sensors the resonance frequency of which detunes with parameter changes, which can be a change in mass [1–5], a change in damping [6,7], or a change in stiffness [8–10]. Resonance-frequency tracking can be accomplished via open- and closed-loop schemes:

(a) The feedback-free (FF) or open-loop approach. In the standard configuration, this scheme has an inferior speed performance when compared to closed-loop and self-adjusting approaches, since it is limited by the mechanical response time of the resonator.

(b) The phase-locked loop oscillator (PLLO) approach. This is commonly used since it can be easily realized digitally with setups based on digital signal processing (DSP) or field-programmable gate arrays (FPGAs). Having a wide frequency range, one setup can be suitable for most micro- and nanomechanical resonators. There are many commercial devices available that can be used for PLLO implementations.

(c) The self-sustaining oscillator (SSO) with positive-feedback approach. The classical realization of the SSO has found limited use, mostly because they are typically implemented as analog circuits, resulting in a narrow frequency range.

The above frequency-tracking schemes have been compared both theoretically [11] and experimentally [12] and it has been concluded that with the closed-loop PLLO and the self-adjusting SSO schemes, better speed performance can be obtained at the expense of degraded precision in the presence of significant transduction noise, as compared to the FF approach. We show that one can, in fact, obtain the same speed versus precision trade-off using the open-loop FF scheme with a simple modification to the standard configuration. The theory behind these approaches has been discussed in depth in Ref. [11]. We also extend the SSO model from Ref. [11] by taking into account the impact of detection noise through two separate mechanisms and show that the resulting frequency fluctuations are equivalent to the PLLO, including the detection-noise-limited regime.

There are various designs for the implementation of the positive-feedback mechanism in the SSO configuration.

*hajrudin.besic@tuwien.ac.at

The most common is to simply amplify and adjust the phase of the resonator response signal to generate the feedback drive, resulting in a sine-driven SSO. Alternatively, amplitude- and duration-adjustable timed pulses can be used in forming the drive for the resonator with a positive-feedback mechanism, resulting in a pulse-driven SSO [13–18]. We have designed and realized an SSO configuration based on the pulsed-feedback mechanism. To experimentally investigate the SSO and the PLLO approaches, we compare our SSO implementation to a DSP- or FPGA-based lock-in amplifier setup with an integrated PLL system.

II. THEORY

A. Noise in nanomechanical resonators

We consider two noise sources, the *thermomechanical* noise of the resonator and the *detection* noise generated in the transduction and detection hardware.

The thermomechanical noise is the most fundamental noise source of the resonator. It can be modeled as a white-noise force $n_{\mathrm{th}}(t)$ at the input of the resonator [11,19] and it has a one-sided spectral density with units of N^2/Hz:

$$S_F = \frac{4m\omega_0 k_B T}{Q}, \tag{1}$$

where k_B is Boltzmann's constant, T is the temperature, m is the effective mass, ω_0 is the eigenfrequency, and Q is the quality factor of the resonator. For a slightly damped resonator, the eigenfrequency is approximately equal to the resonance frequency $\omega_r \approx \omega_0$. The white-noise force at the input of the resonator is shaped by the complex force susceptibility of the resonator,

$$\chi(s) = \frac{1/m}{s^2 + \frac{\omega_0}{Q}s + \omega_0^2}, \tag{2}$$

resulting in a steady-state thermomechanical-amplitude noise at its output with a power spectral density

$$S_{\mathrm{th}}(\omega) = S_F\,|\chi(j\omega)|^2. \tag{3}$$

Operating at resonance, the thermomechanical-amplitude noise reduces to

$$S_{\mathrm{th}} = S_{\mathrm{th}}(\omega_0) = S_F\left(\frac{Q}{m\omega_0^2}\right)^2 = \frac{4k_B T Q}{m\omega_0^3}. \tag{4}$$

The detection noise $n_d(t)$ is produced during the conversion of the mechanical motion into an electrical signal. It includes the noise generated by the readout and electronics. The detection noise can be modeled as a white-noise source with respect to the thermomechanical-amplitude noise:

$$S_d = \mathcal{K}^2 S_{\mathrm{th}}, \tag{5}$$

where $\mathcal{K}$ is a dimensionless factor that corresponds to the ratio between the detection-noise background and the height of the thermomechanical-noise peak. If $\mathcal{K} > 1$, the thermomechanical-noise peak is buried in detection noise. If $\mathcal{K} < 1$, the thermomechanical noise is resolved above the detection-noise background.

The resonator is driven by a coherent force $F(t)$, which results in a steady-state amplitude response at resonance of $x(t) = F(t)Q/(m\omega_0^2) = A_r\cos(\omega_0 t)$ with an amplitude A_r. Both the thermomechanical and the detection-amplitude noise then translate into corresponding phase noise with the following power spectral densities [20]:

$$\begin{aligned} S_{\theta_{\mathrm{th}}} &= \frac{2}{A_r^2}S_{\mathrm{th}}, \\ S_{\theta_d} &= \frac{2}{A_r^2}S_d = \mathcal{K}^2 S_{\theta_{\mathrm{th}}}. \end{aligned} \tag{6}$$

This transformation clearly shows that a large oscillation amplitude A_r dilutes the effect of thermomechanical and detection noise. The maximization of A_r is limited by the onset of nonlinearities in the resonator system.

The conversion of the phase noise [see Eq. (6)] into frequency noise $S_{\Delta\omega}(\omega)$ depends on the tracking scheme and will be derived in the following sections.

B. Feedback-free scheme

The feedback-free (FF) scheme is a simple and well-known method where the resonator is driven at or close to resonance. Figure 1 shows a schematic representation of the FF frequency-tracking scheme. It consists of a signal generator that is driving the resonator with a constant frequency close to its resonance frequency. The resonator motion is then transduced and the phase difference of the resonator response with respect to the reference signal provided by the driving signal generator is obtained by a phase detector (PD). Any sudden change in the resonance frequency, $\Delta\omega_r$, will cause a corresponding change in the detected phase difference $\Delta\theta(t)$, as derived in Ref. [11] as follows:

$$\Delta\theta(t) = \tau_r\Delta\omega_r\left(1 - e^{-t/\tau_r}\right), \tag{7}$$

where

$$\tau_r = \frac{2\,Q}{\omega_r} \tag{8}$$

is the mechanical resonator time constant. The resonance-frequency change $\Delta\omega_r$ can be easily extracted from this

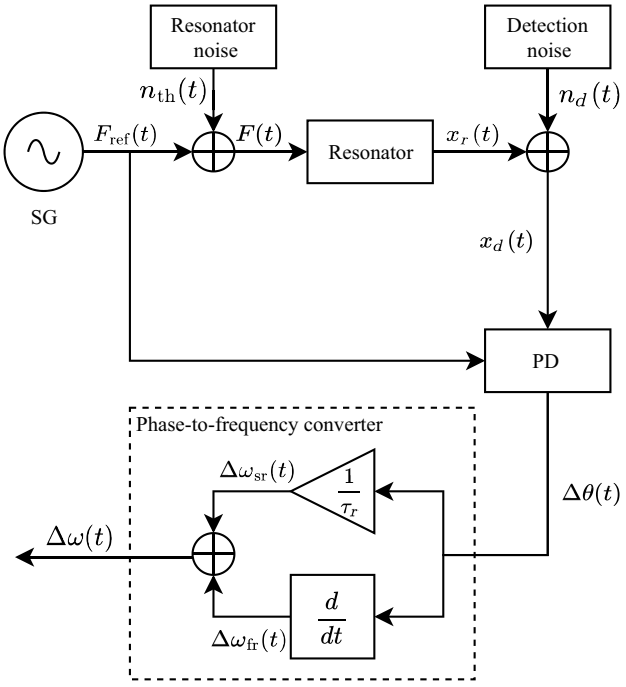

FIG. 1. A block diagram of the FF frequency-tracking scheme, featuring a signal generator (SG) that is driving a micro- or nanomechanical resonator. The resonator response is fed into a phase-difference detector (PD). The phase-difference signal is then mapped to a frequency signal by the phase-to-frequency conversion mechanism. The thermomechanical noise is added at the input of the resonator and the detection noise is added at the input of the phase detector.

phase response. The drawback of the FF scheme is that the drive frequency has to be within the line width of the resonator, where the phase response is linear. This makes this scheme susceptible to thermal drift [11,21]. Here, we assume that the drive signal indeed satisfies this condition for the FF scheme.

The standard map from the phase difference to the resonance-frequency change is obtained simply by a division with τ_r, as described in Ref. [11] and implemented in Ref. [12]. The frequency response in this case, which we call the *slow response*, is given by

$$\Delta\omega_{\rm sr}(t) = \frac{\Delta\theta(t)}{\tau_r} = \Delta\omega_r\left(1 - e^{-t/\tau_r}\right). \tag{9}$$

The slow response contains low-frequency information for resonance-frequency deviations. The speed of the above response is limited by τ_r. For resonators with high quality factors, this response time can become very long.

Alternatively, one can extract the frequency information from the phase $\Delta\theta(t)$ via differentiation (with respect to time), as has been shown in Refs. [22,23]. This results in a *fast* but transient response as follows:

$$\Delta\omega_{\rm fr}(t) = \frac{d\Delta\theta(t)}{dt} = \Delta\omega_r e^{-t/\tau_r}. \tag{10}$$

The fast response contains high-frequency information for resonance-frequency deviations but suppresses low-frequency phenomena such as thermal drift, due to differentiation. By combining (adding) the slow and fast responses, we obtain

$$\Delta\omega(t) = \frac{\Delta\theta(t)}{\tau_r} + \frac{d\Delta\theta(t)}{dt} = \Delta\omega_r \tag{11}$$

as an *instantaneous* and nontransient frequency response, which contains both low- and high-frequency information for resonance-frequency deviations. This instantaneous response will only be smoothed and slowed down by any band-limiting mechanism, e.g., a low-pass filter, in the phase detector. For instance, when phase-difference detection is performed with an in-phase and quadrature (I/Q) demodulator, as in a lock-in-amplifier setup, the response speed will be determined by the low-pass filters in the demodulator, represented by a transfer function $H_L(s)$. The bandwidth for these filters needs to be smaller than (twice) the resonance frequency in order to filter out the high-frequency (at twice the resonance frequency) signal components that are produced by the multipliers in the demodulator. By transforming Eq. (11) into the Laplace domain and including $H_L(s)$ to represent the band-limited nature of phase detection, we obtain

$$H_{\rm FF}(s) = \left(\frac{1}{\tau_r} + s\right) H_L(s), \tag{12}$$

which can be also written as

$$H_{\rm FF}(s) = \frac{1}{\tau_r}\frac{1}{H_r(s)} H_L(s), \tag{13}$$

where $H_r(s)$ is a single-pole low-pass filter with the time constant of the resonator

$$H_r(s) = \frac{1}{1 + s\tau_r}, \tag{14}$$

capturing the input-output frequency-domain response of the resonator. $H_{\rm FF}(s)$ can be used in computing the frequency-domain frequency response of the FF scheme (with combined fast and slow responses) to step changes in the resonance frequency, as well as for characterizing frequency fluctuations due to noise.

The frequency fluctuations caused by noise in the FF scheme are directly determined by the phase fluctuations

of the input signal to the phase detector. The phase fluctuations detected by the phase detector can be expressed in the Laplace domain as

$$\Delta\theta(s) = \theta_{\rm th}(s)H_r(s) + \theta_d(s). \tag{15}$$

The thermomechanical phase fluctuations are shaped by the resonator characteristics before they are detected, while the detection noise is fed into the phase detector unaltered [11]. The frequency fluctuations of the FF tracking scheme are then obtained by simply multiplying the phase fluctuations by the transfer function of the FF scheme,

$$\Delta\omega(s) = \Delta\theta(s)H_{\rm FF}, \tag{16}$$

yielding the transfer functions for the two noise sources:

$$H^{\rm FF}_{\theta_{\rm th}}(s) = \frac{1}{\tau_r}H_L(s),$$
$$H^{\rm FF}_{\theta_d}(s) = \frac{1}{\tau_r}\frac{1}{H_r(s)}H_L(s). \tag{17}$$

C. Self-sustaining oscillator

The standard SSO configuration as shown in Fig. 2 is based on the Barkhausen criterion, which requires that the closed-loop gain is equal to one. This can be achieved by introducing a nonlinearity (a saturating amplifier) $h(\cdot)$ in the loop, which stabilizes the amplitude. This nonlinearity also generates higher-order harmonics, which are well filtered if the resonator has a large quality factor. The Barkhausen criterion also imposes a phase condition for stable and sustained oscillations: the phase around the loop needs to be $n2\pi$, where $n = 1, 2\cdots$ is much smaller than the quality factor of the resonator. The phase condition is realized by introducing a phase-shifting element that phase shifts or delays the signal at the output of the resonator to generate the feedback drive.

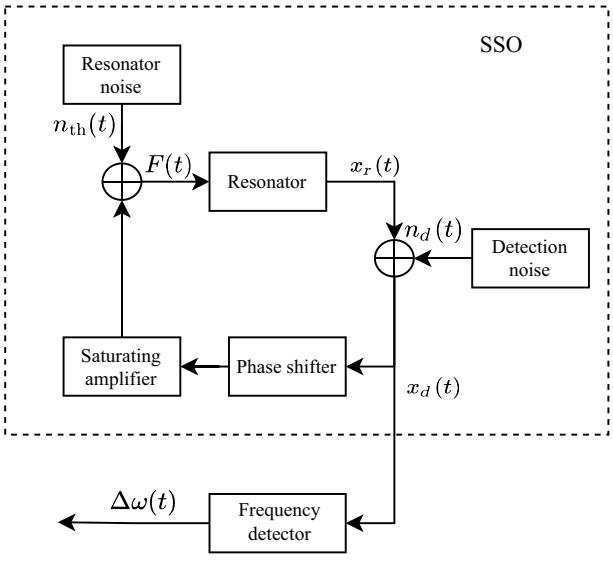

FIG. 2. A block diagram showing a standard SSO scheme, with a phase shifter and a nonlinear saturating element in the positive-feedback path. The thermomechanical-noise force $n_{\rm th}(t)$ is added at the input of the resonator. The detection noise $n_d(t)$ is added in the transduction of the displacement signal $x_r(t)$ into an electrical signal $x_d(t)$. The electrical signal is then filtered and acquired by the frequency detector.

The working principle of a standard SSO is described in Ref. [11], where a model was derived. We start with the following equation from Ref. [11]:

$$\frac{d}{dt}\Delta\theta_r(t) = \frac{1}{\tau_r}\frac{1}{A_{\rm rss}}\frac{Q}{m\omega_r^2}[h(A_{\rm rss})n_d(t) + n_{\rm th}(t)]$$
$$= \frac{1}{\tau_r}\left[\frac{Q}{m\omega_r^2}h(A_{\rm rss})\theta_d(t) + \theta_{\rm th}(t)\right], \tag{18}$$

with the steady-state and noiseless amplitude $A_{\rm rss}$. The above equation describes the fluctuations caused by noise at the resonator output phase and hence in the signal $x_r(t)$ in Fig. 2. Due to the feedback path, detection noise $n_d(t)$ contributes to the phase fluctuations of $x_r(t)$. However, phase fluctuations in the detected resonator output [$x_d(t)$ in Fig. 2] have an additional contribution due to detection noise. Equation (18) can be augmented as follows to derive the equation for phase fluctuations in $x_d(t)$:

$$\frac{d}{dt}\Delta\theta(t) = \frac{1}{\tau_r}\left[\frac{Q}{m\omega_r^2}h(A_{\rm rss})\theta_d(t) + \theta_{\rm th}(t)\right] + \frac{d}{dt}\theta_d(t). \tag{19}$$

As stated in Ref. [11], the gain condition for a self-sustaining oscillator,

$$\frac{Q}{m\omega_r^2}h(A_{\rm rss}) = 1, \tag{20}$$

needs to be met, which yields

$$\frac{d}{dt}\Delta\theta(t) = \frac{1}{\tau_r}[\theta_d(t) + \theta_{\rm th}(t)] + \frac{d}{dt}\theta_d(t). \tag{21}$$

The transfer functions from thermomechanical- and detection-noise sources to the (frequency of the) output $x_d(t)$ can be derived based on the above equation:

$$H^{\rm SSO}_{\theta_{\rm th}}(s) = \frac{1}{\tau_r}H_L(s),$$
$$H^{\rm SSO}_{\theta_d}(s) = \frac{1}{\tau_r}\frac{1}{H_r(s)}H_L(s), \tag{22}$$

where H_r is a single-pole low-pass filter with the time constant of the resonator. H_L has low-pass characteristics and represents the bandwidth-limiting (noise-filtering) mechanism in the frequency-detection device.

D. Phase-locked loop oscillator

The PLLO is essentially a closed-loop extension of the FF scheme, which continually updates the drive frequency to match the resonance frequency of the resonator. The block diagram in Fig. 3 shows the standard PLLO setup with a simplified representation of its internal structure. PLLO is usually realized digitally, e.g., by using a lock-in amplifier with an integrated PLL. The internal oscillator, also called a controlled or local oscillator (LO), of the PLLO drives the resonator. The thermomechanical noise n_{th} is added to the drive at the input of the resonator. The motion of the resonator $x_r(t)$ is transduced into an electrical signal $y(t)$. The electrical signal then goes into a phase detector (PD) and is compared to the internal LO signal. PD is realized with an I/Q demodulator and has internal low-pass filters (LPF) with a cutoff frequency f_L (and time constant $\tau_L = 1/2\pi f_L$). This filter removes high-frequency signal components, as well as high-frequency noise, but limits the bandwidth of phase detection. The output of PD (minus a set point) is used as the error signal $\Delta\theta_e$ that represents the difference in phase between the resonator response and the LO drive signal. The PI controller produces the control signal that sets the frequency of the LO. The negative-feedback loop maintains the desired phase difference between the resonator response and the LO. The speed with which the PI controller regulates the oscillator is characterized in Ref. [19] using the system bandwidth of the PLLO or f_{PLL} [12]. The PI coefficients are calculated from the desired system bandwidth as follows [11]:

$$k_p = 2\pi f_{\text{PLL}} = \frac{1}{\tau_{\text{PLL}}},$$
$$k_i = \frac{k_p}{\tau_r}, \tag{23}$$

where k_p is the proportional coefficient and k_i is the integral coefficient of the PI controller. The noise-transfer functions for the PLLO can be derived based on the loop dynamics as described in Ref. [11]:

$$H^{\text{PLL}}_{\theta_{\text{th}}}(s) = \frac{1}{\tau_r}\frac{(sk_p + k_i)H_L(s)}{s^2 + \frac{s}{\tau_r} + (sk_p + k_i)H_L(s)},$$
$$H^{\text{PLL}}_{\theta_d}(s) = \frac{1}{\tau_r}\frac{1}{H_r(s)}\frac{(sk_p + k_i)H_L(s)}{s^2 + \frac{s}{\tau_r} + (sk_p + k_i)H_L(s)}. \tag{24}$$

With the parameters in Eq. (23), the above noise-transfer functions take the following simpler forms [11]:

$$H^{\text{PLL}}_{\theta_{\text{th}}}(s) = \frac{1}{\tau_r}\frac{H_L(s)}{H_L(s) + s\,\tau_{\text{PLL}}},$$
$$H^{\text{PLL}}_{\theta_d}(s) = \frac{1}{\tau_r}\frac{1}{H_r(s)}\frac{H_L(s)}{H_L(s) + s\,\tau_{\text{PLL}}}. \tag{25}$$

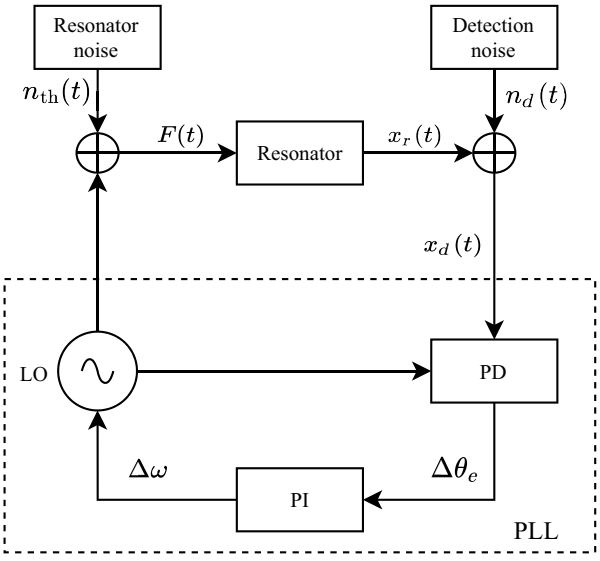

FIG. 3. The phase detector (PD) computes the phase difference between the resonator response and the local oscillator (LO), which (minus a set point) is fed into the PI controller as an error signal. The PI controller tunes the frequency of the LO, which is used to drive the resonator.

E. Allan deviation

The standard and well-established method for characterizing frequency fluctuations is the Allan deviation $\sigma_y(\tau)$ [11,19,24]. It is the square root of the Allan variance, which can be computed with

$$\sigma_y^2(\tau) = \frac{1}{2\,(N-1)}\sum_{i=1}^{N}(y_{i+1,\tau} - y_{i,\tau})^2, \tag{26}$$

where y_i is the ith sample of the averaged frequency over the averaging time τ, i.e.,

$$y_{i,\tau} = \frac{1}{\tau}\int_{(i-1)\tau}^{i\tau} y(t)dt. \tag{27}$$

The frequency values when computing an Allan deviation need to be normalized, resulting in a fractional frequency

$$y(t) = \frac{\Delta\omega(t)}{\omega_0}. \tag{28}$$

The Allan variance can also be computed in the frequency domain if the power spectral density of the fractional

frequency fluctuations is known:

$$\sigma_y^2(\tau) = \frac{1}{2\pi}\frac{8}{\tau^2}\int_0^\infty \frac{\left[\sin\left(\frac{\omega\tau}{2}\right)\right]^4}{\omega^2} S_y(\omega)d\omega. \tag{29}$$

For white frequency fluctuations with $S_y(\omega) = \text{constant}$, Eq. (29) reduces to

$$\sigma_y^2 = \frac{S_y(0)}{2\tau}. \tag{30}$$

Hence, in a system limited by, e.g., thermal white noise, the resulting Allan deviation exhibits a $\sigma_y \propto 1/\sqrt{\tau}$ dependence with the averaging time τ.

The power spectral density of the frequency noise $S_{\Delta\omega}(\omega)$ can be computed as a superposition of the power spectral densities of the thermomechanical and detection phase noise [see Eq. (6)] multiplied with their corresponding transfer functions (magnitude squared) derived above [11], which then readily yields the fractional frequency noise required to compute the Allan deviation:

$$\begin{aligned} S_y(\omega) &= \frac{S_{\Delta\omega}(\omega)}{\omega_0^2} \\ &= \frac{S_{\theta_{\text{th}}}(\omega)|H_{\theta_{\text{th}}}(j\omega)|^2 + S_{\theta_d}(\omega)|H_{\theta_d}(j\omega)|^2}{\omega_0^2} \\ &= \frac{S_{\theta_{\text{th}}}(\omega)}{\omega_0^2}\left[|H_{\theta_{\text{th}}}(j\omega)|^2 + \mathcal{K}^2|H_{\theta_d}(j\omega)|^2\right]. \end{aligned} \tag{31}$$

III. METHODS

The models for the three frequency-tracking schemes were tested experimentally with a nanoelectromechanical system (NEMS) resonator. While the FF and PLLO tracking schemes were implemented with a commercial lock-in amplifier (HF2LI 50-MHz lock-in amplifier from Zurich Instruments), the SSO scheme was realized with a frequency-tracking prototype device from Invisible-Light Labs GmbH.

A. NEMS resonator

The NEMS resonator used in this work (see Fig. 4) consists of a 1018-μm-sized square-membrane-shaped resonator made of 50-nm-thick low-stress silicon-rich silicon nitride (fabricated by low-pressure chemical vapor deposition). The electrical transduction is realized by two 5-μm-wide Au traces passing on the resonator. The membrane is placed in the center of a static magnetic field of about 0.8 T, created by a Halbach array of neodymium magnets, with the traces oriented perpendicular to the magnetic field. Exploiting the resulting Lorentz force, the metal traces can be used both to drive with an ac current and, in return, to detect the motion of the resonator through the magnetomotively induced voltage. The signal from the metal

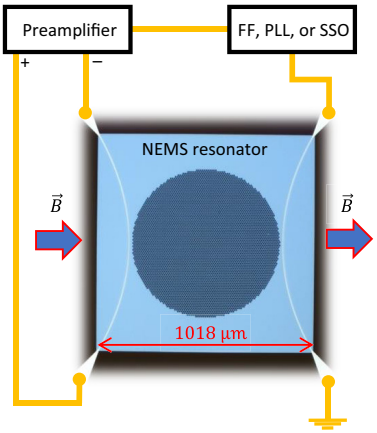

FIG. 4. A schematic of the NEMS resonator used for all experiments featuring electrodynamic transduction. The circular area in the center where the SiN drumhead is perforated has no relevance for this work.

trace for detection is amplified with a low-noise differential preamplifier with a gain factor of 10^4. The NEMS chip is placed in a vacuum chamber featuring a rotary vane pump, reaching a vacuum of 5.2×10^{-3} mbar. With a resonance frequency of $\omega_r = 82.3$ kHZ and a quality factor of $Q = 97\,000$, the NEMS resonator has a response time [see Eq. (8)] of $\tau_r = 2Q/\omega_r = 0.4$ s.

B. SSO with pulsed drive

The SSO frequency-tracking system from Invisible-Light Labs that was used in this work is based on pulsed positive feedback [25,26], producing pulses of width T_w with an adjustable delay T_d with respect to the signal phase θ_0, and a feedback-controlled amplitude to sustain a constant vibrational amplitude of the resonator. A schematic of the timing of the wave forms at the outputs produced by the pulsed positive feedback is shown in Fig. 5.

A narrow pulse with width T_w in the time domain corresponds to a sinc function in the frequency domain with zero points at integer multiples of $f_b = 1/T_w$. The first zero point can be considered as the bandwidth of the pulse. The frequency content above f_b is small in comparison to the ones below f_b and does not contribute much to the signal. Hence, when actuating a resonator, a pulsed signal can be used instead of the typical sinusoidal signal, as is common for, e.g., the characterization of tuning forks [27].

Figure 6 shows the block-diagram representation of the positive-feedback system used in this work. The signal generated by the NEMS resonator is first amplified with a preamplifier before it enters the positive-feedback path. The feedback signal is first passed through a band-pass filter, which serves two purposes. First, it reduces detection noise and, second, it attenuates unwanted modes of the resonator. Afterward, the signal passes through a phase detector, which is able to detect a phase at 0° or 180°. Phase

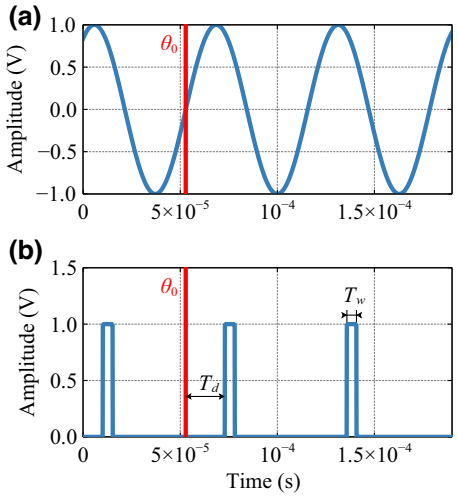

FIG. 5. The timing of the positive-feedback system. (a) The sinusoidal signal at the resonator output is fed into the positive-feedback mechanism. The mechanism detects the phase θ_0. (b) The pulse-generation mechanism generates a pulse with a time delay T_d with respect to θ_0.

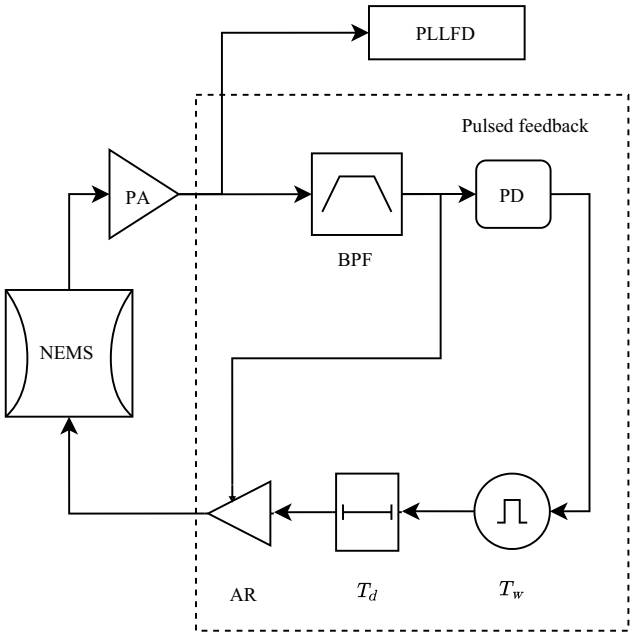

FIG. 6. A block diagram of the pulsed positive-feedback system provided by Invisible-Light Labs used for the SSO scheme. The NEMS resonator response is amplified by a preamplifier (PA) and filtered by a band-pass filter (BPF). The phase is then detected by a phase detector (PD). The pulse generated by the pulse generator is delayed by the delay line. The pulses go through a feedback-controlled amplitude regulation (AR) to drive the NEMS resonator at a fixed vibrational amplitude.

shifts introduced by components in the loop are compensated by an adjustable time-delay element, which induces a delay T_d to the output pulse. T_d needs to be large enough to cover a phase delay between 0° and 180°, which requires a maximum delay of $T_{d,\max} \geq \pi/\omega_r$. The driving pulse is generated via a pulse-generation mechanism that is triggered by the phase detector. The positive-feedback system generates a pulse with adjustable width T_w. Modification of the resonance frequency and therefore the pulse frequency at constant pulse width will result in a change in the energy pumped into the system and hence the amplitude of the resonator will change. This behavior is compensated by regulating the amplitude of the pulse. The amplitude regulation adjusts the pulse height in accordance with the measured input signal level and desired set point.

The amplitude control is performed by the amplitude-regulation block. It measures the amplitude of the signal at the output of the band-pass filter and compares it to the desired set point.

To adjust the output voltage to the required NEMS voltage values, a 100-dB attenuator is placed at the output of the positive feedback. The band-pass filter, amplitude regulation, T_d, and T_w are adjustable parameters.

C. Tracking-schemes setup

For the PLLO scheme, the desired system target bandwidth is determined by the PI coefficients with the relations in Eq. (23). The low-pass filter bandwidth f_L of the PLLO demodulator is set 5 times larger than the target bandwidth. The sampling rate is set at least 10 times larger than the LPF bandwidth.

In order to compare the tracking schemes, the sensor needs to be driven at its resonance. In the case of the SSO, the delay of the pulse was adjusted until the phase of the pulses matched the phase of the resonator. This is obtained when the maximum oscillation amplitude is reached for a fixed pulse amplitude. In the case of the PLLO, to lock onto the phase that corresponds to the resonance frequency, a frequency sweep needs to be performed. This sweep is also needed to determine the resonance and hence the drive frequency for the FF scheme. To make sure that the resonator has the same vibrational amplitude for all tracking schemes, the drive amplitude was set so that in all schemes, the output of the preamplifier had the same amplitude of 22.1 mV. The PLLO dynamics are determined by the chosen target bandwidth. The dynamics of the FF approach are limited by the demodulation-filter bandwidth in the phase detector. While the SSO core itself exhibits an instantaneous response to sudden resonance-frequency changes, the dynamics are limited by the frequency-detection device that is used in conjunction with the SSO [11].

While the pulsed positive-feedback device comes with a built-in frequency counter, in this work to provide a one-to-one comparison between the different schemes, a PLL-based frequency detector (PLLFD) was also used for the SSO scheme. The controlling signal for the local oscillator

of the PLL was then used to measure the frequency of oscillation of the SSO core. This is in contrast to the use of a PLL in the PLLO scheme, where the local oscillator signal in fact drives the resonator and its frequency is locked to the resonance frequency by maintaining the appropriate phase difference between the resonator output and the drive. Using the same PLL frequency detection allows us to set the system response time to be equal for all three of the tracking schemes.

IV. RESULTS AND DISCUSSION

A. Analytical results

Figure 7 shows the theoretical Allan deviations for the three frequency-tracking schemes. The Allan deviation for a NEMS resonator that is limited by thermomechanical and detection noise exhibits two regimes with slopes proportional to $1/\tau$ and $1/\sqrt{\tau}$. A $1/\tau$ slope arises from (amplified) detection noise, whereas the more fundamental thermomechanical noise results in a $1/\sqrt{\tau}$ slope, as expected for a white-noise source [see Eq. (30)]. Equation (31) indicates that the functional form of the Allan deviation is determined by two factors. The first is the ratio between the detection and the thermomechanical noise, $\mathcal{K}$. As shown in Fig. 7(a), increasing $\mathcal{K}$ increases the relative impact of detection noise, resulting in the change of the slope from $1/\sqrt{\tau}$ to the $1/\tau$. The second factor that affects the Allan deviation is the system bandwidth f_L, which acts as a low-pass filter for signal variations. In all tracking schemes, which all use an I/Q demodulator for phase detection, signal variations are filtered by the low-pass filter inside the demodulator. In the PLLO scheme and in the PLLFD used in conjunction with the SSO, there is additional filtering due to the negative-feedback-loop dynamics with a bandwidth f_{PLL}. In practice, the demodulator bandwidth is set larger than the loop bandwidth ($f_L \geq 5\, f_{\mathrm{PLL}}$). For the calculations presented in Fig. 7, the bandwidths were chosen equal, at $f_L = f_{\mathrm{PLL}}$, to obtain an equal overall bandwidth for all schemes. Since a first-order demodulator filter in PLLO and SSO PLLFD effectively results in an overall second-order filter due to the loop dynamics, a second-order demodulator filter is used in the FF scheme to obtain the same effective filter order for all three schemes.

Figure 7(b) shows the effect of changing the filter bandwidth f_L on the Allan deviation. Decreasing f_L improves the filtering of detection noise and results in a smaller Allan deviation–at the expense, however, of a larger response time [11,12].

It is important to point out that even though thermomechanical noise is resolved above the detection-noise background ($\mathcal{K} < 1$) for all calculations presented in Fig. 7, detection noise can nonetheless affect the resulting Allan deviations. As is shown in Fig. 7(a), frequency fluctuations do not start to reach the thermomechanical-noise limit with a $1/\sqrt{\tau}$ slope until $\mathcal{K} \leq 0.001$. This behavior can be ascribed to the long response time of the high-Q NEMS resonator. This finding underlines the importance of a low-noise readout that provides a highly resolved thermomechanical-noise peak to obtain minimal frequency fluctuations with high-Q resonators.

B. Experimental testing

The frequency fluctuations for the different tracking schemes were studied by collecting the steady-state frequency data over 1 min. The corresponding Allan-deviation curves calculated from the frequency data are presented in Figs. 8(a)–8(c). The integrated electronic transduction of the NEMS resonator could not resolve its thermomechanical-noise peak, resulting in $\mathcal{K} \gg 1$. The corresponding theoretical Allan-deviation curves are plotted in Figs. 8(d)–8(f).

The FF measurements shown in Fig. 8(a) were performed with a second-order demodulation filter with the

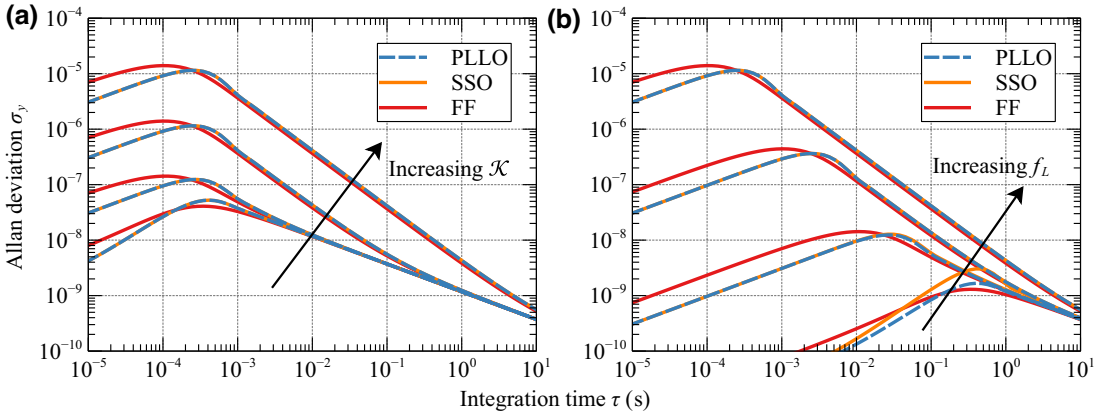

FIG. 7. Theoretical Allan deviations for the three frequency-tracking schemes for (a) increasing detection noise ($\mathcal{K} = \{10^{-4}, 10^{-3}, 10^{-2}, 10^{-1}\}$) for a fixed bandwidth $f_L = 1$ kHz and (b) increasing system bandwidth ($f_L = \{1\text{ Hz}, 10\text{ Hz}, 100\text{ Hz}, 1\text{ kHz}\}$) for a fixed $\mathcal{K} = 0.1$. All calculations were performed for a resonator time constant $\tau_r = 0.4$ s.

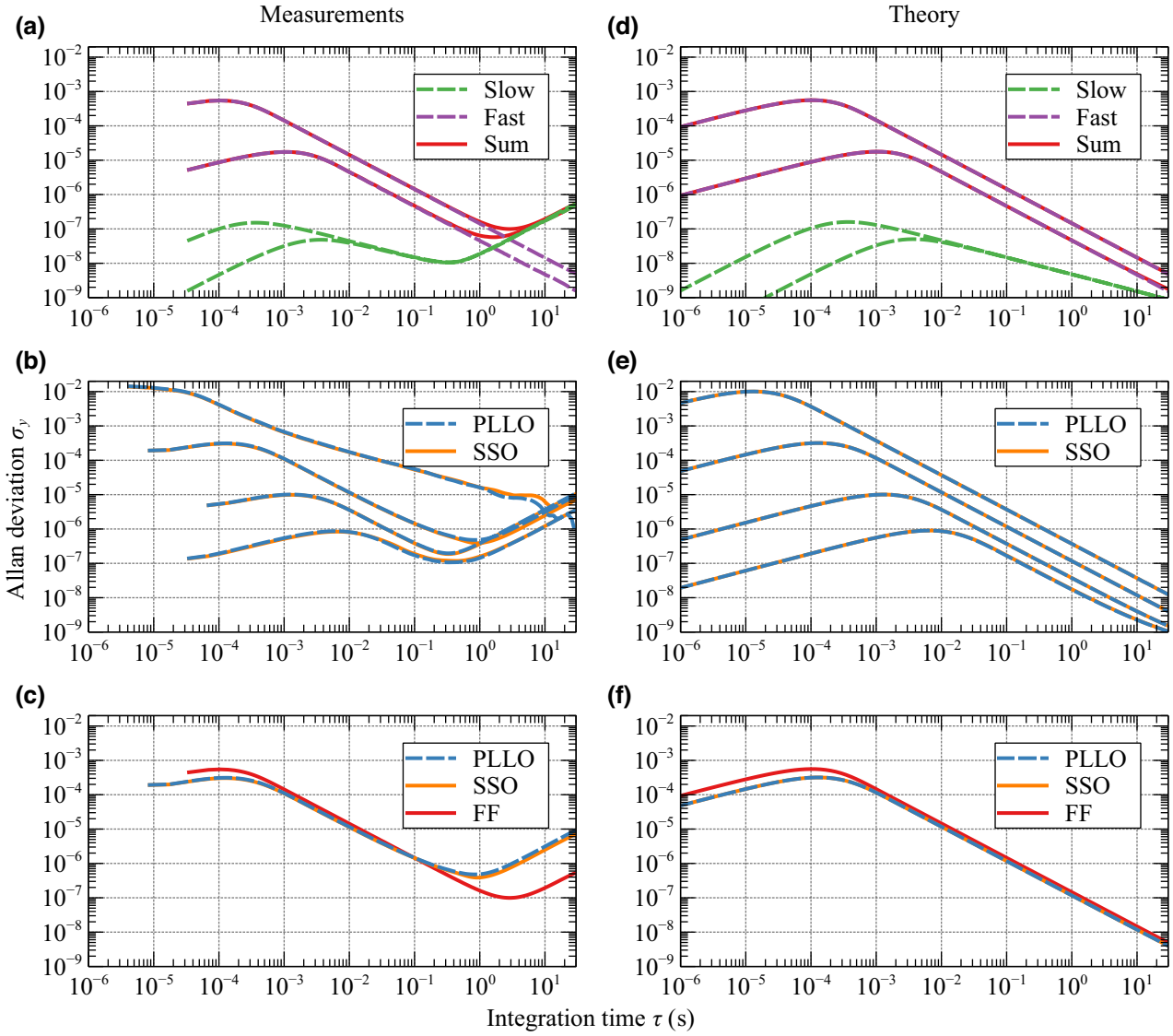

FIG. 8. A comparison of the experimental Allan deviations with theory. (a) The Allan deviations for three FF tracking modes with second-order demodulation filters of bandwidth $f_L = \{100\ \text{Hz}, 1\ \text{kHz}\}$. (b) A comparison of the PLLO and SSO tracking schemes for $f_{\text{PLL}} = \{10\ \text{Hz}, 50\ \text{Hz}, 500\ \text{Hz}, 5\ \text{kHz}\}$, where a PLLFD is used as the frequency detector for the SSO scheme. (c) A comparison of PLLO and SSO with $f_{\text{PLL}} = 500$ Hz and the FF scheme (combined or sum mode) with $f_L = 1$ kHz. (d)–(f) Theoretical model-based computations using Eqs. (29) and (31) for the same settings as in the measurements (a)–(c) and with calibration for the detection-noise level.

cutoff frequencies $f_L = \{100\ \text{Hz}, 1\ \text{kHz}\}$. The experimental results show that the FF scheme in slow mode has a slope proportional to $1/\sqrt{\tau}$. Changing the filter bandwidth does not affect the precision performance of this scheme, because, in the slow mode, the limiting and determining factor is the mechanical time constant of the resonator. On the other hand, in the fast mode, the Allan deviation has a $1/\tau$ slope, pointing to the fact that precision is determined by (amplified) detection noise. With a larger filter bandwidth, the response becomes faster but at the expense of less precision, indicated by a larger Allan deviation. It can also be observed that due to its high-pass but *low-stop* nature, the fast response does not contain information about slow processes such as thermal drift. Combining the slow and fast responses, according to Eq. (11), results in an Allan deviation that exhibits low-frequency phenomena, while the response speed is limited only by the demodulation filter. The experimental Allan deviations can be recreated with high accuracy by the theoretical model, which is plotted in Fig. 8(d).

For the PLLO and SSO-PLLFD schemes shown in Fig. 8(b), measurements were performed for four different loop bandwidths, $f_{\text{PLL}} = \{10\ \text{Hz}, 50\ \text{Hz}, 500\ \text{Hz}, 5\ \text{kHz}\}$, with a demodulation low-pass filter cutoff $f_L = 5\ f_{\text{PLL}}$.

The PI-controller parameters were chosen according to Eq. (23). In this case, the closed-loop dynamics for the PLLFD of the SSO and the PLLO are almost equivalent, especially when $f_{\mathrm{PLL}}\ \tau_r \gg 1$. Having the same filtering characteristics and response times for both tracking schemes, a fair comparison can be made. We observe that the Allan deviations for SSO PLLFD and PLLO are almost identical for all system bandwidths. As the theory indicates, with increasing bandwidth, the amplification of detection noise becomes more severe and Allan deviations with $1/\tau$ dependence in the detection-noise-limited regime become worse. For $f_{\mathrm{PLL}} = 5$ kHz ($f_L = 25$ kHz) and a sampling rate of 230 kSa/s, a premature $1/\sqrt{\tau}$ dependence can be observed with an even worse Allan deviation. This behavior is a result of the practical limitation of the digital PLL. This arises if the sampling rate is not at least 10–20 times larger than the demodulator low-pass filter bandwidth, to prevent aliasing. It should be noted that, in the model-based theoretical computations, it is assumed that the sampling rate is large enough to prevent aliasing in Allan-deviation computations. There is almost perfect correspondence between the measurements and the model-based computations, presented in Fig. 8(e), for smaller bandwidths, when there is no aliasing.

Figure 8(c) shows the Allan deviations for the FF (combined fast and slow response), PLLO, and SSO-PLLFD tracking schemes for a similar system bandwidth. Clearly, all of the measured Allan-deviation curves are practically identical. The theoretical model, shown in Fig. 8(f), confirms that there is no difference in terms of performance between the three tracking schemes.

All experimental Allan deviations (except for fast-mode FF) exhibit a thermal-drift-related rise for large τ. This is not present in the theoretical computations since thermal drift is not modeled.

V. CONCLUSIONS

In this work, we have extended the existing models for the FF and SSO tracking schemes. We have shown that when the FF tracking scheme is operated in the sum mode (combining the fast and slow response) proposed in this work, it offers speed versus accuracy trade-off characteristics equivalent to those of the closed-loop SSO and PLLO schemes. This is achieved by combining (adding) the slow and fast frequency responses that can be obtained by simple processing of the phase output from the demodulator. We have also demonstrated that the SSO scheme has the same frequency fluctuation performance as the PLLO scheme. Finally, we have compared the FF, SSO, and PLLO tracking schemes and shown that all the tracking schemes have equivalent steady-state frequency fluctuation performance. There are two main parameters that affect the performance of all tracking schemes: (1) the ratio between the thermomechanical-noise peak and the detection-noise floor, $\mathcal{K}$; and (2) the filtering properties of the detection device. We have further shown that a self-sustaining oscillator tracking scheme with a pulsed drive performs perfectly according to the theoretical model of sinusoidal positive feedback. These results give the user an option to choose the tracking scheme based on cost, robustness, ease of implementation, and usability in practice instead of fundamental differences in performance.

ACKNOWLEDGMENTS

We would like to thank Andreas Kainz and Franz Keplinger for constructive discussions that gave us motivation for designing the system described in the paper. This work received funding from the European Innovation Council under the European Union Horizon Europe Transition Open program (Grant Agreement No. 101058711-NEMILIES).

[1] J. Chaste, A. Eichler, J. Moser, G. Ceballos, R. Rurali, and A. Bachtold, A nanomechanical mass sensor with yoctogram resolution, Nat. Nanotechnol. **7**, 301 (2012).

[2] M. S. Hanay, S. Kelber, A. Naik, D. Chi, S. Hentz, E. Bullard, E. Colinet, L. Duraffourg, and M. Roukes, Single-protein nanomechanical mass spectrometry in real time, Nat. Nanotechnol. **7**, 602 (2012).

[3] T. P. Burg, M. Godin, S. M. Knudsen, W. Shen, G. Carlson, J. S. Foster, K. Babcock, and S. R. Manalis, Weighing of biomolecules, single cells and single nanoparticles in fluid, Nature **446**, 1066 (2007).

[4] J. Lee, W. Shen, K. Payer, T. P. Burg, and S. R. Manalis, Toward attogram mass measurements in solution with suspended nanochannel resonators, Nano Lett. **10**, 2537 (2010).

[5] S. Schmid, M. Kurek, J. Q. Adolphsen, and A. Boisen, Real-time single airborne nanoparticle detection with nanomechanical resonant filter-fiber, Sci. Rep. **3**, 1 (2013).

[6] M. Khan, S. Schmid, P. E. Larsen, Z. J. Davis, W. Yan, E. H. Stenby, and A. Boisen, Online measurement of mass density and viscosity of pL fluid samples with suspended microchannel resonator, Sens. Actuators B: Chem. **185**, 456 (2013).

[7] S. Bose, S. Schmid, T. Larsen, S. S. Keller, P. Sommer-Larsen, A. Boisen, and K. Almdal, Micromechanical string resonators: Analytical tool for thermal characterization of polymers, ACS Macro Lett. **3**, 55 (2014).

[8] T. Larsen, S. Schmid, L. Grönberg, A. Niskanen, J. Hassel, S. Dohn, and A. Boisen, Ultrasensitive string-based temperature sensors, Appl. Phys. Lett. **98**, 121901 (2011).

[9] M.-H. Chien, M. Brameshuber, B. K. Rossboth, G. J. Schütz, and S. Schmid, Single-molecule optical absorption imaging by nanomechanical photothermal sensing, Proc. Nat. Acad. Sci. **115**, 11150 (2018).

[10] M. Kurek, M. Carnoy, P. E. Larsen, L. H. Nielsen, O. Hansen, T. Rades, S. Schmid, and A. Boisen, Nanomechanical infrared spectroscopy with vibrating filters for pharmaceutical analysis, Angew. Chem. **129**, 3959 (2017).

[11] A. Demir, Understanding fundamental trade-offs in nanomechanical resonant sensors, J. Appl. Phys. **129**, 044503 (2021).
[12] P. Sadeghi, A. Demir, L. G. Villanueva, H. Kähler, and S. Schmid, Frequency fluctuations in nanomechanical silicon nitride string resonators, Phys. Rev. B **102**, 214106 (2020).
[13] M. Domínguez, J. Pons-Nin, J. Ricart, A. Bermejo, and E. FiguerasCosta, A novel *sigma-delta* pulsed digital oscillator (PDO) for MEMS, IEEE Sens. J. **5**, 1379 (2005).
[14] S. Schmid, P. Senn, and C. Hierold, Electrostatically actuated nonconductive polymer microresonators in gaseous and aqueous environment, Sens. Actuators A: Phys. **145**, 442 (2008).
[15] A. Brenes, J. Juillard, L. Bourgois, and F. V. Dos Santos, Influence of the driving waveform on the open-loop frequency response of MEMS resonators with nonlinear actuation schemes, J. Microelectromech. Syst. **25**, 812 (2016).
[16] J. Juillard, A. Brenes, M. Gouspy, and M. Kraft, in *2019 Symposium on Design, Test, Integration & Packaging of MEMS and MOEMS (DTIP)* (IEEE, 2019), p. 1.
[17] J. Juillard, A. Somma, and A. Brenes, in *2021 IEEE International Symposium on Inertial Sensors and Systems (INERTIAL)* (IEEE, 2021), p. 1.
[18] S. Gorreta, D. Fernandez, E. Blokhina, J. Pons-Nin, V. Jimenez, D. O'Connell, O. Feely, J. Madrenas, and M. Dominguez, Pulsed digital oscillators for electrostatic MEMS, IEEE Trans. Circuits Syst. I: Regular Papers **59**, 2835 (2012).
[19] S. Schmid, L. G. Villanueva, and M. L. Roukes, *Fundamentals of Nanomechanical Resonators* (Springer, Cham, 2023), 2nd ed.
[20] A. Demir and M. S. Hanay, Fundamental sensitivity limitations of nanomechanical resonant sensors due to thermomechanical noise, IEEE Sens. J. **20**, 1947 (2020).
[21] T. R. Albrecht, P. Grütter, D. Horne, and D. Rugar, Frequency modulation detection using high-q cantilevers for enhanced force microscope sensitivity, J. Appl. Phys. **69**, 668 (1991).
[22] R. Giridharagopal, G. E. Rayermann, G. Shao, D. T. Moore, O. G. Reid, A. F. Tillack, D. J. Masiello, and D. S. Ginger, Submicrosecond time resolution atomic force microscopy for probing nanoscale dynamics, Nano Lett. **12**, 893 (2012).
[23] B. Boashash, Estimating and interpreting the instantaneous frequency of a signal. I. Fundamentals, Proc. IEEE **80**, 520 (1992).
[24] F. Walls and D. Allan, Measurements of frequency stability, Proc. IEEE **74**, 162 (1986).
[25] M. Dominguez, J. Pons, J. Ricart, J. Juillard, and E. Colinet, Linear analysis of the influence of FIR feedback filters on the response of the pulsed digital oscillator, Analog Integr. Circuits Signal Process. **53**, 145 (2007).
[26] Éric Colinet, J. Juillard, S. Guessab, and R. Kielbasa, Actuation of resonant MEMS using short pulsed forces, Sens. Actuators A: Phys. **115**, 118 (2004).
[27] E. Schrüfer, L. Reindl, and B. Zagar, in *Elektrische Messtechnik*, p. 1.